Sensors & Diagnostics

PAPER

View Article Online
View Journal | View Issue



Cite this: *Sens. Diagn.*, 2025, **4**, 1024

# Liquid crystal-based optical platform for the detection of colon and breast cancer cell lines using folic acid-conjugated gold nanoparticles

Anupama Kadam, [a] Rajendra Patil,[b] Sneha Mahalunkar,[c] Muthupandian Ashokkumar, [d] Ratna Chauhan*[e] and Suresh Gosavi *[adf]

In the present study, we report for the first time a liquid crystal-based biosensor for the highly sensitive and specific detection of colon and breast cancer cells using folic acid-conjugated gold nanoparticles (FA@GNPs) as the recognition element. FA@GNPs were immobilized on a glass substrate coated with *N*-dimethyl-*N*-octadecyl-3-aminopropyltrimethoxysilyl chloride (DMOAP), which induces homeotropic alignment of the liquid crystal molecules. Folate receptors, which are overexpressed in various cancer types, including colon and breast cancer cells, facilitate the selective binding of these cells to FA@GNPs. This binding event disrupts the vertical alignment of the liquid crystal molecules, causing a distinct transition from a dark to a bright state, which is observable *via* polarizing optical microscopy. Quantitative analysis of the cancer cells was performed by calculating the average grayscale intensity of the optical images, demonstrating that the proposed cell detection platform can sensitively detect individual cancer cells. The proposed liquid crystal biosensor utilizing FA@GNPs as the detection element offers a simple, cost-effective, label-free platform with exceptional specificity and sensitivity for early cancer detection. This novel approach holds significant potential for the development of advanced diagnostic tools in oncological research.

Received 25th June 2025,
Accepted 24th August 2025

DOI: 10.1039/d5sd00111k

rsc.li/sensors



## 1. Introduction

For many decades, research has been directed to developing new techniques in cancer research, mainly in the area of early-stage detection, enabling early cancer therapy, which will help reduce the mortality rate. According to the World Health Organization 2020 report, ~20 million people are diagnosed with cancer, with ~10 million deaths annually.[1] Colon cancer and breast cancer are the leading causes of cancer-related deaths worldwide.[2,3] The early-stage detection of any cancer is very important to reduce the mortality rate. Traditional methods for colon cancer detection frequently involve invasive procedures, which may lack the sensitivity needed for early diagnosis. Hence, there is a demand for the development of novel, non-invasive diagnostic techniques that offer high sensitivity and specificity.

In recent years, biosensors have emerged as a promising tool for the detection of different types of cancer.[4–7] Among the biosensing platforms reported recently, liquid crystal-based biosensors have attracted great attention due to their unique properties such as the ability to translate molecular interactions into optical signals. In the past two decades, researchers have devoted significant efforts to fabricating liquid crystal-based biosensors for the detection of diverse analytes such as multiple viral respiratory viruses,[8] HBD-2 (human β-defensin-2),[9] sulfadimethoxine,[10] DNA,[11] pathogens,[12] glucose,[13] cecropin B,[14,15] dopamine,[16] bovine serum albumin (BSA),[17] cholesterol,[18] and malathion.[19] However, despite the versatility and promise of liquid crystal-based biosensors, there remains a noticeable gap in reported studies specifically on cancer cell detection. H. Pourasl *et al.* reported the detection of HER-2 cancer biomarkers using human epidermal growth factor receptor-2 (ref. 20) and Hassanein *et al.* detected the cancer biomarker CA125 based on lyotropic chromonic liquid crystals.[21] C. Tsung-Keng *et al.* proposed a liquid crystal biosensor for the label-free detection of a single circulating tumor cell[22] and H. Su *et al.* developed a biosensor

[a] *Department of Physics, Savitribai Phule Pune University, Pune-411007, India. E-mail: swg@physics.unipune.ac.in*
[b] *Department of Biotechnology, Savitribai Phule Pune University, Pune-411007, India*
[c] *School of Basic Medical Science, Savitribai Phule Pune University, Pune-411007, India*
[d] *School of Chemistry, University of Melbourne, VIC 3010, Australia*
[e] *School of Nano Science, Central University of Gujrat, Kundhela-391107, Vadodara, India. E-mail: ratnasingh.bhu@gmail.com*
[f] *Photocatalysis International Research Centre, Research Institute for Science & Technology, Tokyo University of Science, 2641 Yamazaki, Noda, Chiba 278-8510, Japan*

for the detection of the cancer biomarker CA125.[23] These liquid crystal-based biosensors offer several advantages such as label-free detection with high sensitivity and potential for miniaturization, making them suitable for diagnostics.

Folic acid (FA) is a small molecule ligand with high affinity for the folate receptors present cancer cells. It has been reported that folate receptors are overexpressed on cancer cells, which hints that folic acid is suitable as a recognition agent.[24,25] It is has also been reported that folate receptors are expressed in breast, colon, ovarian, cervical and endometrial cancers.[26,27]

HT-29 cells have been widely reported to overexpress folic acid receptors. Studies, such as Kalli *et al.* (2008), have demonstrated that FR expression is elevated in colorectal cancer, including HT-29 cells, making them an appropriate model for folic acid-based targeting approaches in both therapeutic and diagnostic applications[28] (Kalli KR, *et al.*, 2008, Clinical Cancer Research). Alternatively, although MDA-MB-231 cells have FR, studies such as Lu *et al.* (2013) have reported detectable levels of folic acid receptor-alpha (FR-α) under specific experimental conditions, indicating their utility for folic acid-based targeting[29] (Lu Y, *et al.*, 2013, Cancer Letters). Moreover, receptor-mediated uptake has been demonstrated for folic acid-functionalized nanoparticles in MDA-MB-231 cells, supporting their suitability for these studies.

The integration of liquid crystal technology with these recognition agents offers several advantages for the detection of colon and breast cancer, which provides a label-free and simplified detection process at reduced cost.

This research focuses on the development and application of a liquid crystal-based biosensor for the detection of colon cancer cells. By harnessing the specific molecular interactions between cancer biomarkers and recognition elements immobilized on the biosensor surface, this platform aims to provide a sensitive and rapid detection method for colon cancer cells and breast cancer cell in biological samples.

Herein, we present a novel liquid crystal-based cell detection platform designed for the detection of colon cancer and breast cancer cells. The cell detection platform utilizes folic acid-functionalized gold nanoparticles (FA@GNP) as recognition elements, which have high affinity and specificity towards colon and breast cancer cells overexpressing folate receptors. The unique optical properties of liquid crystals allow the real-time monitoring of interactions between FA@GNP and the target colon and breast cancer cells, enabling rapid and sensitive detection. In this paper, we discuss the process for the fabrication of the liquid crystal-based cell detection platform, the optimization of FA@GNP as the recognition element, and the evaluation of the cell detection platform performance in detecting colon and breast cancer cells under a polarizing optical microscope. Furthermore, its potential as a promising tool for early-stage cancer diagnosis is highlighted.

Overall, the development of this liquid crystal-based cell detection platform represents a significant advancement in the field of cancer diagnostics, offering a sensitive, label-free, and real-time detection platform for the early detection of cancer cells. Liquid crystal molecules are highly responsive to changes in their environment, including temperature, electric field, and surface interactions. Liquid crystal-based biosensors have gained significant attention in recent years due to their sensitivity, versatility, and potential for the real-time monitoring of various biological molecules. These biosensors employ the unique properties of liquid crystals to transduce biological interactions into measurable signals.

## 2. Experimental

### 2.1 Materials

The nematic liquid crystal (LC) 4-cyano-4′-pentylbiphenyl (5CB), *N*,*N*-dimethyl-*N*-octadecyl-3-aminopropyltrimethoxysilyl chloride (DMOAP), gold(III) chloride trihydrate ($HAuCl_4$), sodium trisodium citrate, dimethyl sulfoxide (DMSO), 1-ethyl-3-(3-dimethylaminopropyl) carbodiimide (EDC), and *N*-hydroxysuccinimide (NHS) were obtained from Sigma-Aldrich. The commercial colon cancer cell line HT-29 was provided by Skanda Life Sciences, Bangalore. The commercial breast cancer cell line MDA MB 231 was provided by the National Centre for Cell Science, Pune. Ultrapure water was used throughout the experiments.

### 2.2 FA@GNP formulation

For the detection of cancer cells, folic acid binds to the surface of GNPs, and a schematic illustration of FA conjugation on the surface GNPs is shown in Fig. 1. In the first step, GNPs were synthesized using a modified method reported by D. Wenchao *et al.*[30] The synthesized GNPs were coated by PVP polymer, which is amphipathic in nature. The hydrophobic end of PVP polymer initially binds to the surface of GNPs and its hydrophilic end remains free in the medium, which is then reacted with EDC. EDC acts as a crosslinking agent with free amine groups on the surface of GNPs. In the second step, folic acid is activated by EDC/NHS, and due to this, the stable NHS-ester is formed. Finally, when the NHS-ester moiety interacts with the free amine group present on the PVP-coated GNPs, it forms amide bond and coupling occurs to obtain FA@GNPs.

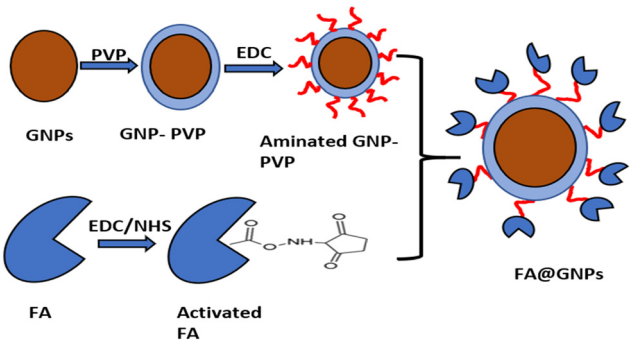


Fig. 1 Schematic of FA conjugation on the surface of GNPs.

### 2.3 Preparation of LC cell substrate

To prepare the sensing substrate, a series of cleaning and decoration steps was followed. Firstly, glass substrates were cleaned using a piranha solution, which was prepared by adding 30 mL of concentrated $H_2SO_4$ to 10 mL of $H_2O_2$. The glass substrates were immersed in the solution for 1 h, and then rinsed thoroughly three times with distilled water, and stored at 110 °C overnight to ensure complete drying. Subsequently, the cleaned glass slides underwent decoration with dimethyloctadecyl[3-(trimethoxysilyl)propyl]ammonium chloride (DMOAP). This involved immersing the glass slides in an aqueous solution containing 0.4% (v/v) DMOAP at room temperature for 1 h, followed by rinsing three to four times with distilled water. Then the slides were heated at 110 °C overnight to facilitate uniform surface modification and stored under dry conditions for further use. To fabricate the sensing substrate for cancer cell detection, 0.5 mL of a folic acid-functionalized gold nanoparticle (FA@GNP) solution was drop-cast onto the DMOAP-coated glass slides and allowed to dry overnight at room temperature. After drying, the slides were rinsed with distilled water to remove any unbound nanoparticles, ensuring a selective FA@GNP layer for subsequent interactions. For cancer cell detection, varying concentrations of colon cancer cells ranging from 1 μL to 10 μL (approximately 5–8 cell per μL), as well as a high-density concentration of 1 μL (10 000 cells per

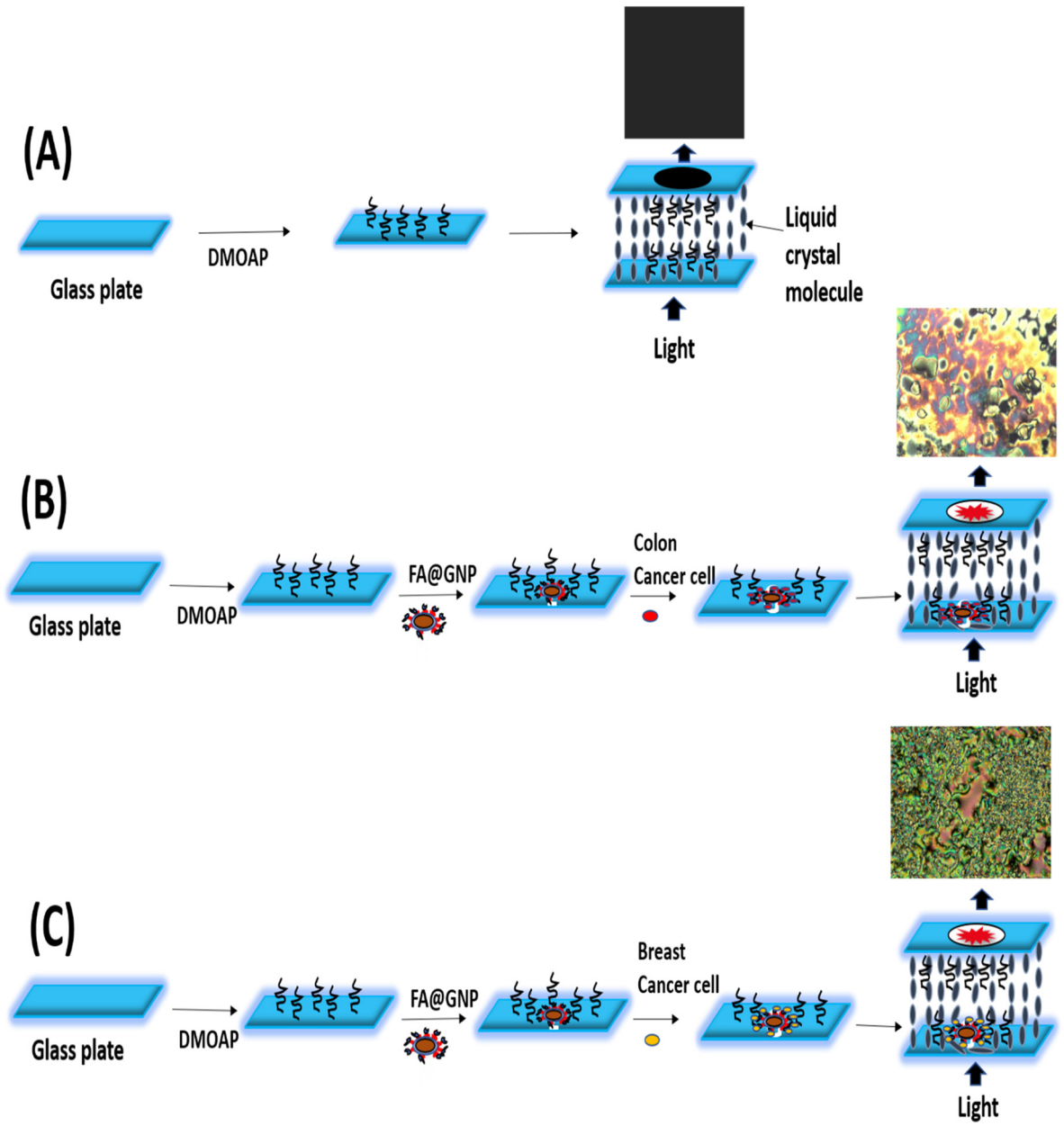


Fig. 2 Schematic of the preparation steps of the liquid crystal cell detection platform for cancer cell detection.

μL), were drop-cast onto the FA@GNP-decorated glass substrates. Similarly, breast cancer cells ranging from 1 μL to 10 μL (5–8 cell per μL) were drop-cast onto the FA@GNP-decorated glass substrates. The cells were incubated on the substrates for 2 h, allowing specific binding interactions, after which the slides were rinsed with distilled water to remove unbound cells and dried at room temperature. The liquid crystal (LC) cell was prepared by assembling two glass slides spaced with a 20 μm Mylar spacer and sealed with araldite glue. The top glass slide was modified with DMOAP, while the bottom slide was decorated with cancer cells and FA@GNPs as the sensing substrate. An additional LC cell was fabricated by spacing a DMOAP-decorated glass slide and an FA@GNP-coated sensing substrate with a 20 μm Mylar spacer, and sealed similarly with Araldite glue. To ensure consistency, the spacing was verified using a micrometer screw gauge. Nematic liquid crystals (NLCs) were then drawn into the LC cell *via* capillary action above the NLC isotropic transition temperature, achieving homogeneous filling. Optical images of the assembled LC cells were captured under crossed polarizers using a polarized optical microscope equipped with a digital camera (Fig. 2).[31]

### 2.4 Detection principle of cell detection platform

The sensing mechanism of the proposed liquid crystal cell detection platform for the detection of breast cancer cells and colon cancer cells is illustrated schematically in Fig. 2. For the fabrication of the cancer cell detection platform, the sensing substrate was prepared by coating FA@GNPs on a DMOAP-coated glass plate. Coating of DMOAP provides vertical homeotropic alignment to the liquid crystal molecule, which results in a dark background in POM (Fig. 2(A)). Then, different concentrations of colon cancer cells and breast cancer cells were drop-cast on the sensing substrate. It has been reported that folate receptors (FRa, FRb and FRc) are cysteine-rich cell-surface glycoproteins that bind folate with high affinity.[32] Due to the overexpression of folate receptors on colon and breast cancer cells, these cancer cells bind to the folate-conjugated GNPs. After the specific binding between the folate-conjugated GNPs and cancer cells, the surface morphology of the sensing substrate changes greatly and disturbs the orientation of the LC molecules (Fig. 2(B) and (C)).

### 2.5 Characterization

The optical absorption spectra of GNPs and folate-conjugated GNPs were recorded using a JASCO V-670 UV-vis spectrophotometer. Zeta potential was measured using a Malvern Zetasizer 7.13 version. Transmission electron microscopy (TEM) was conducted on GNPs and folate-conjugated GNPs using a TECNAI G220 instrument equipped with EDS attachment, operated at 200 kV. The interaction between GNPs and folate-conjugated GNPs was investigated through transmission Fourier-transform infrared (FTIR) spectroscopy using a JASCO FT/IR 6100 series instrument. Analysis of the alignment and uniformity of the liquid crystal (LC) molecules was studied using a polarizing optical microscope (POM), specifically an Eclipse Ci-POL by Nikon Corporation, configured with a crossed polarizer-analyzer arrangement. POM images were captured using a CCD camera.

The surface topology of the substrate assembled with DMOAP, folate-conjugated GNPs and cancer cells was studied using atomic force microscopy (AFM). The AFM image was obtained in contact mode at a scan rate of 1.2 Hz in the scan range of 2.5 μm × 2.5 μm. The water contact angles of the substrates modified with DMOAP and folate-conjugated GNPs were measured using an automated optical contact angle (OCA) goniometer system and analysed with the SCA 20 software (DataPhysics Instruments, Germany). The contact angle was recorded using an automated optical contact angle (OCA) goniometer system and analysed using the SCA 20 software (Data Physics Instruments, Germany).

## 3. Result and discussion

### 3.1 UV-visible spectra of GNPs and folate conjugated GNPs

The UV-visible spectra of GNPs revealed a surface plasmon resonance peak at 522 nm, a characteristic feature of GNPs (Fig. 3). When coated with PVP polymer, a minor red shift of 1 nm was observed, confirming the successful coating of PVP onto the GNPs. The GNP-PVP complex, post-functionalization with EDC cross-linking agent, readily allows conjugation to various biomolecules and ligands, particularly FA. Upon EDC functionalization of GNP-PVP, the absorbance spectrum shifted to 527 nm. The free folic acid shows characteristic absorption peaks at 307 nm and 355 nm, while FA@GNPs exhibit peaks at 270 nm and 448 nm. The observed shift in absorption confirms the successful conjugation, while the presence of characteristic features supports the retention of the optical signature of folate after conjugation. The two absorption peaks at 270 nm and 348 nm indicate an interaction between the folate molecule and GNPs. This observation confirms the covalent attachment of folate to the GNPs.[33] Furthermore, the UV-visible spectrum of FA-conjugated GNP-PVP exhibited a surface plasmon band at around 563 nm, supporting the fact that folate is conjugated or attached to the surface of the gold nanoparticles. The red shift in the plasmon band provides additional evidence of the successful conjugation of folate with the GNPs.[34]

### 3.2 Zeta potential

Zeta potential is a measure of the surface charge of nanoparticles in suspension, and it reflects the stability of the particles in solution. The zeta potential of GNPs is −26.8 mV and FA@GNPs is −8.01 mV, as shown in Fig. S2(A and B), respectively. The significant change in zeta potential from −26.8 mV to −8.01 mV indicates that the folate molecules are effectively conjugated to the surface of the GNPs, altering their surface charge and stability. Initially, citrate-capped GNPs carry a strong negative surface charge due to the presence of citrate ions. However, folic acid itself has both carboxyl and amine functional groups, which can interact with the surface of

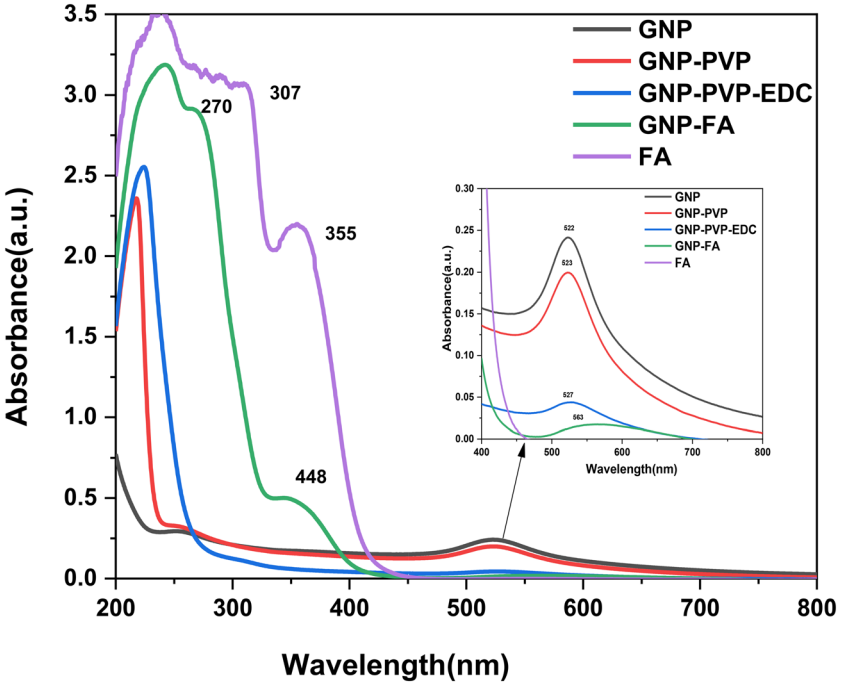


Fig. 3 UV-visible spectra of GNP and folate-conjugated GNPs.

GNPs in a way that neutralizes some of its surface charge, resulting in a reduction in the overall zeta potential. This reduction is a common observation when functionalizing nanoparticles with biomolecules and can actually serve as an indirect confirmation of successful surface modification. This reduced zeta potential reflects the modification of the surface properties, potentially making the GNPs more suitable for biological applications, where interactions with cell membranes and proteins are influenced by surface charge.[35]

### 3.3 FTIR spectra of GNPs and FA-GNPs

The FTIR spectra of GNPs and FAGNPs are presented in Fig. 4. The FTIR spectrum of GNPs with peaks at 3386 $cm^{-1}$, 1630

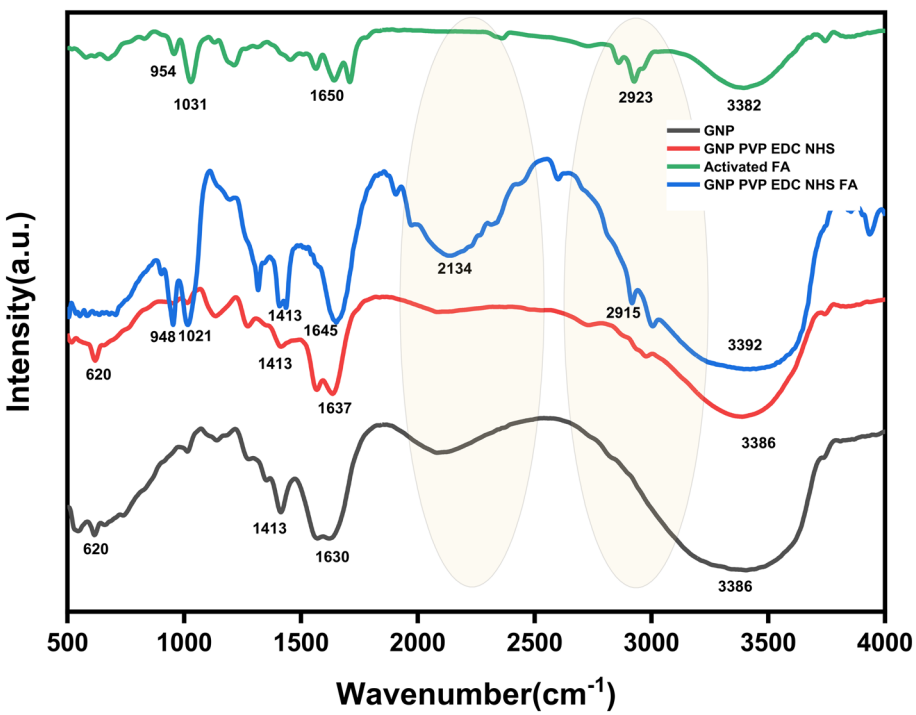


Fig. 4 FTIR spectra of GNP and folate-conjugated GNPs.

$cm^{-1}$, 1413 $cm^{-1}$, and 620 $cm^{-1}$ provides information about the molecular composition and bonding characteristics of the nanoparticles. The peak at 3386 $cm^{-1}$ is due to the presence of hydroxyl groups, which is associated with water molecules or surface-bound hydroxyl groups on the GNPs. The peak at 1630 $cm^{-1}$ can be attributed to the C=C stretching vibrations, suggesting the presence of unsaturated carbon–carbon bonds. The peak at 1413 $cm^{-1}$ is associated with the $CH_3$ bending. The peak at 620 $cm^{-1}$ is due to (Au–O) stretching, which is associated with the metal-oxygen stretching vibrations, indicating the interaction between gold and oxygen atoms. The FTIR spectrum of folic acid shows peaks at 3382 $cm^{-1}$, 2923 $cm^{-1}$, 1650 $cm^{-1}$, 1031 $cm^{-1}$, and 954 $cm^{-1}$. The peak at 3382 $cm^{-1}$ is associated with hydroxyl (OH) stretching. The peak at 2923 $cm^{-1}$ is associated with alkane stretching vibrations, representing the presence of aliphatic hydrocarbon chains in the folic acid molecule. The peak at 1650 $cm^{-1}$ corresponds to the amide I band, revealing the presence of C=O stretching vibrations in the amide group of folic acid. The peak at 1031 $cm^{-1}$ is attributed to the C–O stretching vibrations, which suggest the presence of ether or alcohol groups in the folic acid molecule. The peak at 954 $cm^{-1}$ corresponds to the C–H bending vibrations in the aromatic rings. The analysis of the FTIR spectrum of the folate-conjugated GNPs reveals important information about the functional groups present in the sample.[36] The peaks observed at 3392 $cm^{-1}$, 2915 $cm^{-1}$, 2134 $cm^{-1}$, 1645 $cm^{-1}$, 1413 $cm^{-1}$, 1021 $cm^{-1}$, and 948 $cm^{-1}$ provide insights into the molecular structure and bonding characteristics of the folate-conjugated GNPs. The peak at 3392 $cm^{-1}$ shows the presence of hydroxyl groups. The peak at 2915 $cm^{-1}$ is associated with alkane stretching vibrations, which are due to the presence of aliphatic hydrocarbons or CH groups in the folate-conjugated GNPs. The peak at 1645 $cm^{-1}$ corresponds to the amide I band, indicating the presence of proteins or peptides. The peak at 1413 $cm^{-1}$ is related to methyl ($CH_3$) bending vibrations. The peak at 1021 $cm^{-1}$ is due to C–O stretching vibrations. This could be associated with the conjugation of folate, which often involves its attachment through oxygen-containing functional groups. The peak at 948 $cm^{-1}$ corresponds to C–H bending vibrations, likely associated with alkynes or aromatic rings.[37] This indicates the structure of the folate molecule on the GNP. The FTIR spectrum of the gold nanoparticles conjugated with folate exhibits distinctive peaks related to diverse functional groups, offering crucial insights into the composition and structure of the conjugated nanoparticles. The presence of peaks with slight shifts, corresponding to folic acid and GNPs, serves as confirmation of the successful conjugation of folate on the surface of the gold nanoparticles.[38]

### 3.4 TEM and EDS analysis

The morphology, size, and distribution of the synthesized GNPs and folate-conjugated GNPs were examined using the transmission electron microscopy (TEM) technique, as shown in Fig. 5. The TEM images of the GNPs reveal their spherical nature with nearly uniform sizes (Fig. 5A). Similarly, the TEM images of the folate-conjugated GNPs, denoted as folate@GNPs, demonstrate spherical shapes with a high degree of size uniformity (Fig. 5B). Notably, in the TEM images of both GNPs and folate-conjugated GNPs, observable contrast differences arise due to the presence of folate ligands on the surface of the nanoparticles. This contrast variation provides visual confirmation of the successful conjugation of folate onto the gold nanoparticles, and it underscores the potential influence of the folate ligands on the overall appearance of the GNPs in the TEM images.

Energy-dispersive X-ray spectroscopy (EDX) proves helpful in verifying the successful binding of folate to the surface of GNPs. By conducting EDX analysis on the folate-conjugated GNPs, distinct bands characteristics of GNPs are identified (Fig. 5C). Additionally, the detection of elements such as carbon (C), nitrogen (N), and oxygen (O) corresponding to the FA molecule strongly suggests the effective functionalization of GNPs with folic acid. This observation further supports the conclusion that the binding of folate to the GNP surface has been achieved.[39]

### 3.5 Optimization of folate@GNP concentration for enhanced sensing substrate performance

The development of an effective sensing substrate requires meticulous optimization of the folate@GNP concentration on a DMOAP-decorated glass plate. As illustrated in Fig. 6, concentrations exceeding 5 μg $mL^{-1}$ have been observed to disrupt the alignment of homeotropic liquid crystals, compromising the sensing performance of the substrate. However, at concentrations of 1 μg $mL^{-1}$, 2 μg $mL^{-1}$, and 5 μg $mL^{-1}$ of folate@GNP, the homeotropic alignment of the liquid crystal molecules remains undisturbed. This preservation of alignment is evidenced by the acquisition of a dark image in the polarizing image of the assembled LC cells captured under crossed polarizers using a polarized optical microscope, indicating a stable and suitable configuration for sensing applications. Considering these findings, the concentration of 5 μg $mL^{-1}$ of folate@ GNPs has been carefully selected for the formulation of the sensing substrate. This particular concentration not only ensures the preservation of the homeotropic alignment critical for sensing functionality but also strikes a balance that avoids the disruptions observed at higher concentrations. The careful consideration of optimal concentration is essential in achieving a robust and reliable sensing platform, thus enhancing the overall performance and accuracy of the sensing substrate.

### 3.6 Impact of FA@GNP and cancer cell interaction on surface morphology of DMOAP-coated substrate

The surface morphology of the DMOAP-coated glass plate after incubation with FA@GNP and colon cancer cells is depicted in Fig. 7. The DMOAP-coated substrate initially exhibits a relatively uniform and smooth structure. Upon incubation with FA@GNP, a slight increase in surface roughness

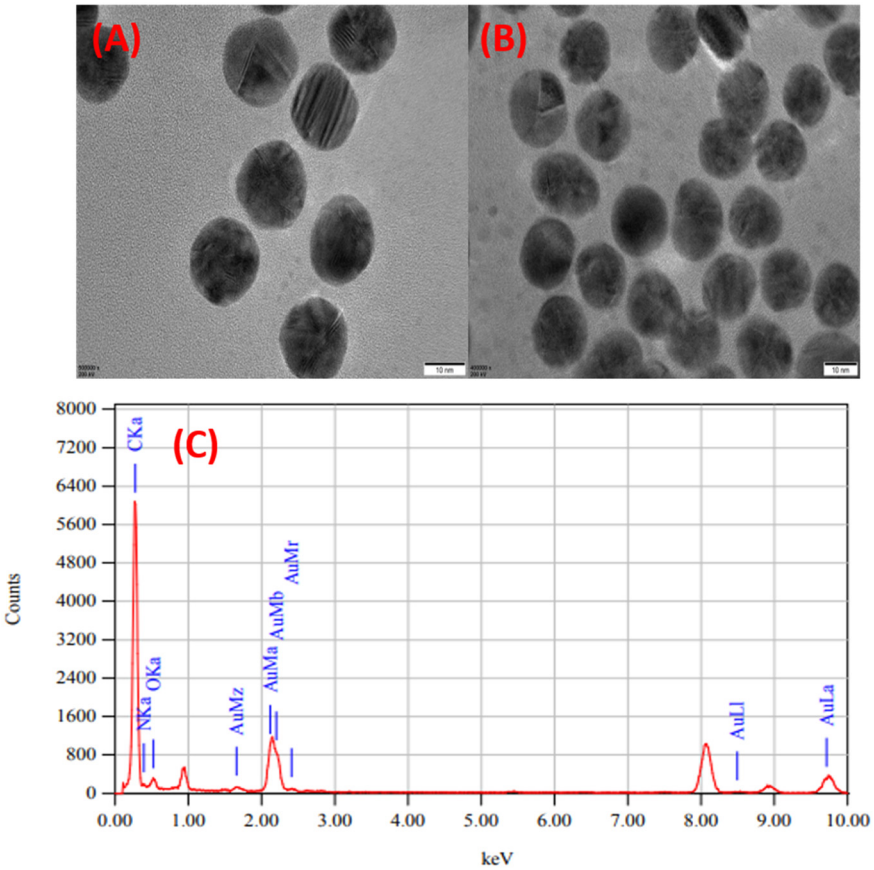


**Fig. 5** (A) TEM image of GNPs, (B) TEM image folate-conjugated GNPs, and (C) EDS of folate-conjugated GNPs.

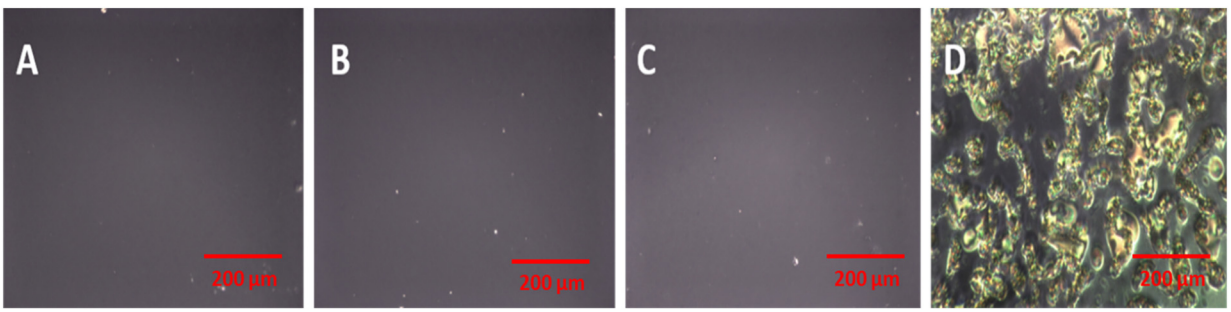


**Fig. 6** Optical images (under crossed polarizer) of LC cells in the presence of different concentrations of folate@GNP (A) 1 μg mL$^{-1}$, (B) 2 μg mL$^{-1}$, (C) 5 μg mL$^{-1}$ and (D) 10 μg mL$^{-1}$.

is observed compared to the unmodified DMOAP-coated substrate. This minor alteration suggests the successful adsorption of FA@GNP on the surface without significant disruption of the substrate integrity. However, when the DMOAP-coated substrate is exposed to colon cancer cells, a notable increase in surface roughness is observed, indicating pronounced interactions between the cells and the FA@GNP-modified substrate. Similarly, in the presence of breast cancer cells, the surface roughness is significantly altered, demonstrating the sensitivity of the substrate to different types of cancer cells. These changes in surface morphology indicate cellular adhesion and proliferation on the substrate, which can affect the performance of the sensing platform. The observed variations in roughness provide valuable insights into the responsiveness of the substrate to biological interactions, which is critical for the development of reliable and efficient biosensing applications.

To evaluate the capturing efficiency of our sensing substrate, we incubated approximately 20 cancer cells of each type (breast cancer cells and colon cancer cells) on the substrate and performed a washing step after 2 h. The capturing rate was calculated using the following formula:

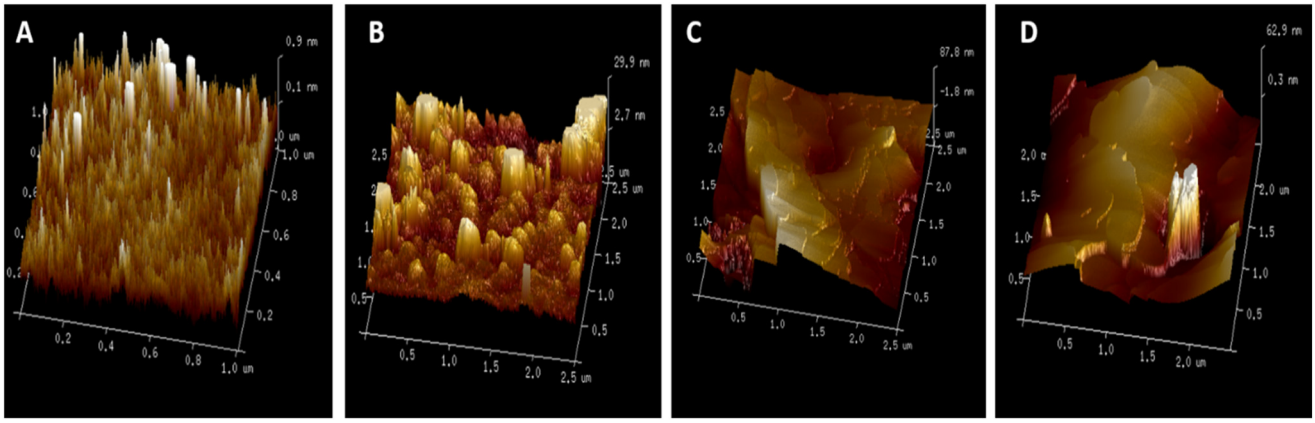


Fig. 7 AFM images of (A) DMOAP, (B) FA@GNP, (C) colon cancer cells, and (D) breast cancer cells.

$$\text{Capturing Rate (\%)} = (\text{Captured Cell Total/Cells Incubated}) \times 100$$

The capturing rate of breast cancer cells is ~90% and colon cancer cells is ~96.66%.

### 3.7 Optical response of liquid crystals to FA@GNP-modified substrates for colon cancer cell detection

Fig. 8(A) shows the optical images of DMOAP decorated on a glass slide, which provides homeotropic alignment for NLC, resulting in a uniform dark background. When the optimal amount of FA@GNP is added to the DMOAP-decorated glass slide, which also results in a dark background, this means that FA@GNP does not disturb the homeotropic alignment of NLC (Fig. 8(B)). Colon cancer cells can be bound to the sensing substrate through the specific binding between FA@GNPs and the folate receptor present on colon cancer cells. Fig. 8(D) to (J) shows optical images of the 0 to 100 000 colon cancer cells per 1 μL DMSO. The orientation of the LC molecule is highly sensitive to the surface topological structure of the substrate. When colon cancer cells were added to the FA@GNP-coated sensing substrate, the surface topology of substrate changed greatly. This change in surface topology disturbed the homeotropic alignment of LC and resulted in the birefringent texture in the optical images of the LC cells. When a solution of 0 cells/1 μL DMSO was added to the LC, the homeotropic alignment of the LC molecules is not disturbed and results in a dark background. Fig. 8(D–I) show the optical images of colon cancer cells with a concentration of 1 μL to 10 μL (5–8 cells/1 μL), which disturb the homeotropic alignment of the LC molecules and result in a birefringent texture in the optical images. Birefringence was observed in the optical images with an increase in the concentration of colon cancer cells. For a higher concentration of colon cancer cells, *i.e.* 1 μL (10 000 cells/1 μL), the homeotropic alignment of the LC molecules is highly disturbed and a completely bright optical image is observed (shown in Fig. 8(J)). Birefringence is observed in the optical image for a low concentration of colon cancer cells, *i.e.* for 1 μL (5–8 cells/1 μL). This indicates that even a low number of cancer cells can induce localized disturbance in the liquid crystal alignment, leading to a detectable optical response in their immediate vicinity, which proves that the LC-based sensor for cancer cell detection is highly sensitive.

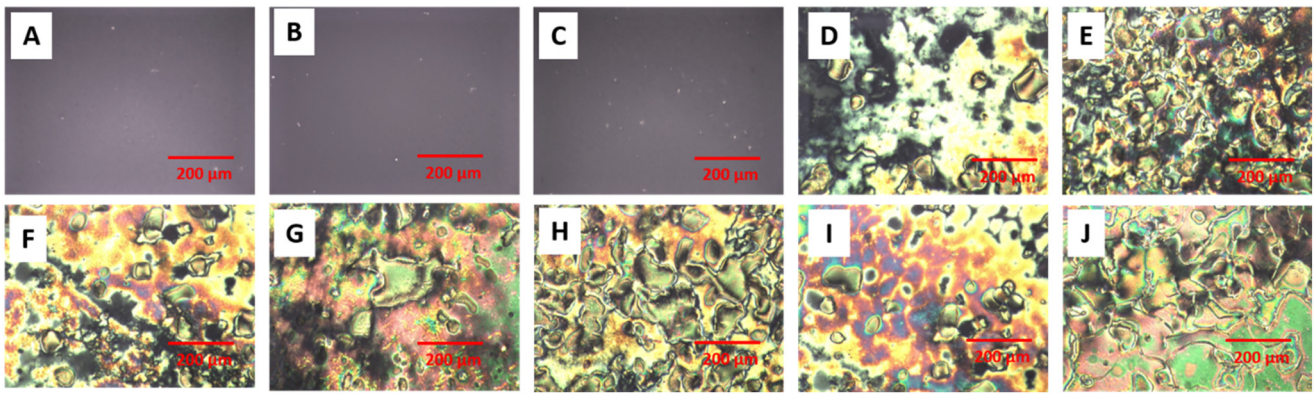


Fig. 8 Optical images (under crossed polarizer) of LC cells. (A) Nematic liquid crystal, (B) FA@GNP, (C) DMSO, (D) 1 μL (1 colon cancer cell/1 μL), (E) 2 μL (1 colon cancer cell/1 μL), (F) 4 μL (1 colon cancer cell/1 μL), (G) 6 μL (1 colon cancer cell/1 μL), (H) 8 μL (1 colon cancer cell/1 μL), (I) 10 μL (1 colon cancer cell/1 μL), and (J) 1 μL (10 000 colon cancer cell/1 μL).

### 3.8 Detection of breast cancer cells using FA@GNP-modified sensing substrate

To evaluate the detection capabilities of the FA@GNP-modified sensing substrate for breast cancer cells, an experiment was performed using varying concentrations of breast cancer cells ranging from 1 μL to 10 μL (5–8 cells $\mu L^{-1}$). These cells were immobilized on FA@GNP-coated glass plates, and their interactions with the liquid crystal (LC) alignment were observed using polarized optical microscopy (POM). As shown in Fig. 9, the POM images demonstrate that the presence of breast cancer cells significantly disrupts the homeotropic alignment of the LC molecules on the substrate.[40] This disruption manifests as a birefringent texture in the optical images, indicating the loss of uniform dark background typically associated with undisturbed LC alignment. The degree of birefringence increases with the concentration of breast cancer cells, suggesting that even a small number of cells can effectively alter the LC orientation. These findings highlight the high sensitivity of the FA@GNP-modified LC-based sensor in detecting breast cancer cells, given that the optical response is strongly correlated with the cell concentration.

In contrast to the folic acid-functionalized GNPs (FA@GNPs), the bare GNPs did not induce any significant LC reorientation upon exposure to the breast cancer cells and colon cancer cells, as shown in Fig. S1. This lack of LC response clearly supports the hypothesis that the FA–folate receptor interaction is critical for the triggering mechanism in our system.

This control experiment confirms that the LC reorientation observed in our study is specifically driven by the targeted interaction between folic acid on the GNPs and the folate receptors on the cancer cell surface, rather than non-specific adsorption or interaction of GNPs with the cells.

### 3.9 Quantitative analysis of LC cell detection platform sensitivity using average gray-scale intensity

To quantitatively evaluate the performance of the liquid crystal (LC) cell detection platform, we analyzed the average gray-scale intensity of the polarized optical microscopy (POM) images obtained for varying concentrations of colon cancer cells and breast cancer cells. The analysis of the average gray-scale intensity of the polarized images involves a systematic protocol to ensure accuracy and reproducibility. Firstly, the polarized images are captured using a polarized optical microscope equipped with a digital camera under consistent lighting conditions to avoid variations in intensity. The captured images are then converted to gray-scale format to eliminate any color-based interference. A specific region of interest within the image, typically corresponding to the area of interaction or alignment changes, is selected for analysis. Image analysis the ImageJ software is commonly employed to calculate the average gray-scale intensity within the region of interest. Specifically, a fixed area of 100 × 100 $\mu m^2$ was selected for grayscale quantification across all images to ensure consistency. Fig. 10 and 11 illustrate the corresponding average gray-scale intensities for the colon cancer and breast cancer cell lines, respectively.

In the colon cancer cells, as depicted in Fig. 10, the average gray-scale intensity of the POM images exhibits a clear upward trend with increasing cell concentrations, ranging from 1 μL to 10 μL (5–8 cells per μL). This trend is characterized by a strong linear correlation, with a coefficient of determination ($R^2$) of 0.91986. This linear relationship suggests that the response of the cell detection platform is proportional to the concentration of colon cancer cells present, making it feasible to quantitatively detect and analyze the concentration of colon cancer cells based on the gray-scale intensity of the POM images.

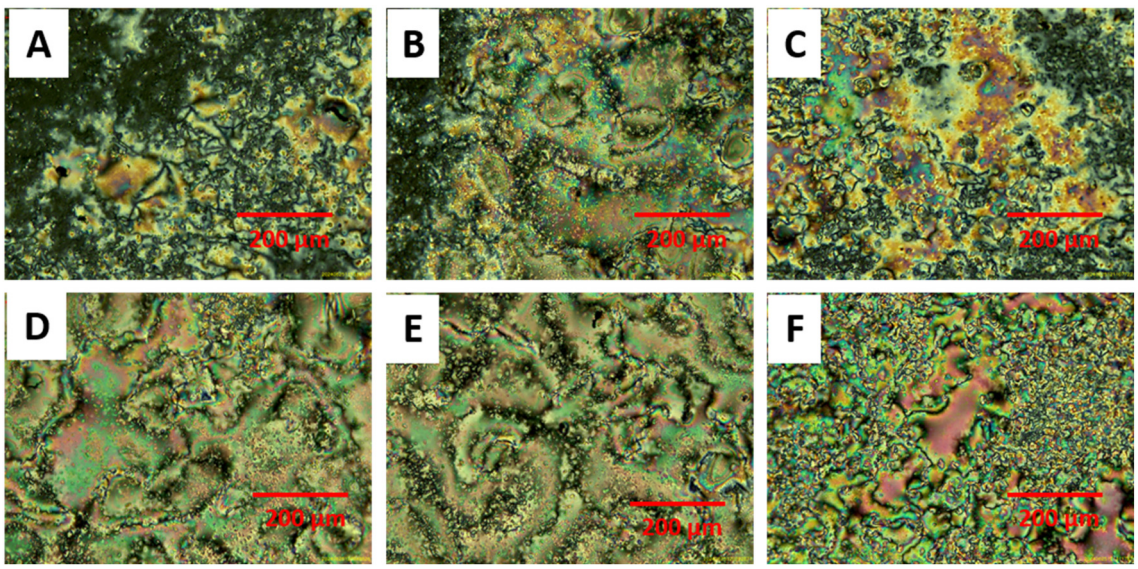


Fig. 9 Optical images (under crossed polarizer) of LC cells. (A) 1 μL (1 breast cancer cell/1 μL), (B) 2 μL (1 breast cancer cell/1 μL), (C) 4 μL (1 breast cancer cell/1 μL), (D) 6 μL (1 breast cancer cell/1 μL), (E) 8 μL (1 breast cancer cell/1 μL), and (F) 10 μL (1 breast cancer cell/1 μL).

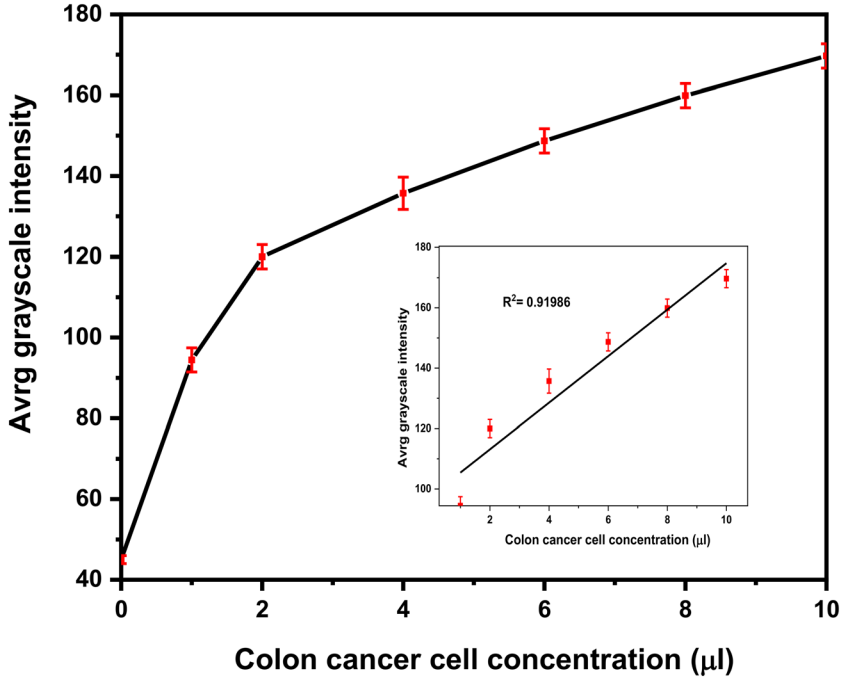


**Fig. 10** Correlations between the average gray-scale intensities of optical images under crossed polarizers of colon cancer cell concentrations. Inset: linear relationship between the gray-scale intensities and the colon cancer cell concentrations.

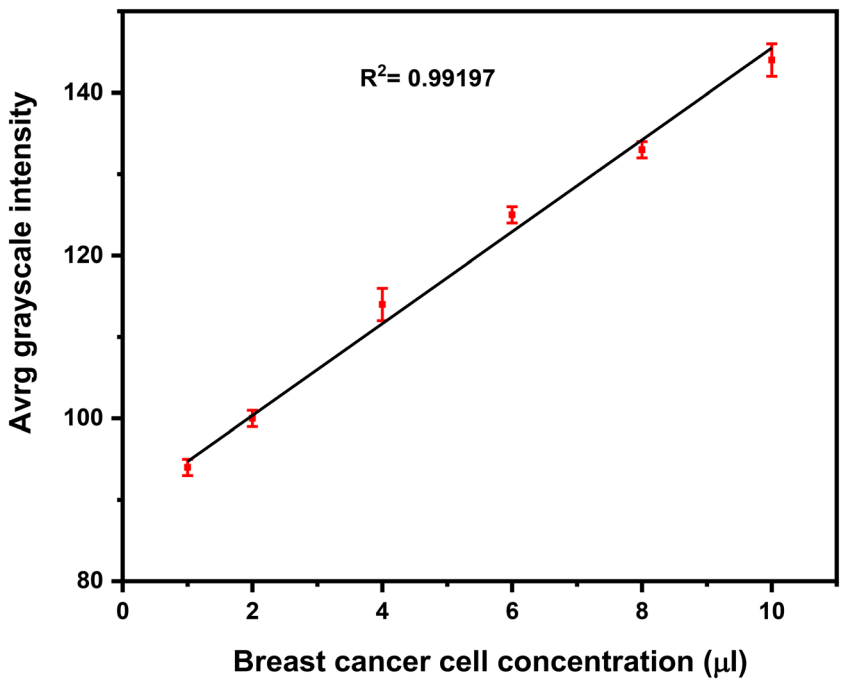


**Fig. 11** Linear relationship between the gray-scale intensity and the breast cancer cell concentration.

Similarly, in the case of breast cancer cells, Fig. 11 demonstrates a highly linear relationship between the average gray-scale intensity of the POM images and the concentration of breast cancer cells. The correlation coefficient ($R^2$) is remarkably high at 0.99197, indicating the excellent linearity and sensitivity of the LC cell detection platform to varying concentrations of breast cancer cells. This high correlation suggests that the sensor can accurately and reliably detect even minimal changes in breast cancer cell concentration, confirming the robustness of

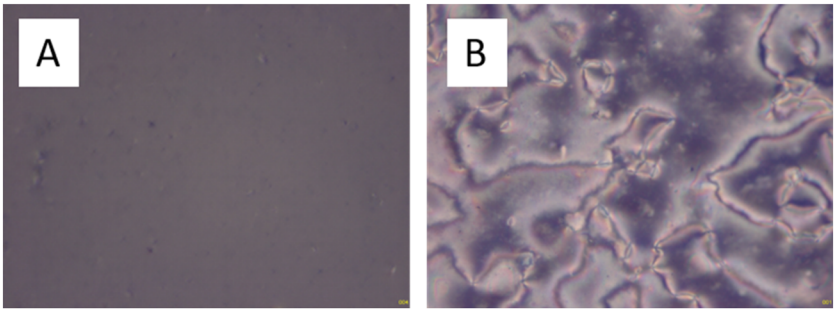


Fig. 12 Optical images of (A) washed normal cells and (B) unwashed normal cells.

the LC cell detection platform for breast cancer cell detection.

Overall, the results indicate that the developed LC cell detection platform can be utilized for the quantitative detection of both colon cancer and breast cancer cells, with significant sensitivity to even single-cell concentrations. The strong linear correlation between gray-scale intensity and cell concentration validates the potential of this cell detection platform for precise and effective cancer cell detection, thereby highlighting its application for early-stage cancer diagnostics and monitoring. Although the current study utilized serial dilutions to estimate the detection sensitivity, incorporating replicate measurements and statistical analyses in future work will further enhance the robustness and reproducibility of the results. These efforts will strengthen the quantitative reliability of the platform and support its advancement toward clinical application as a sensitive and accessible tool for early cancer diagnostics.

### 3.10 Specificity testing of FA@GNP-coated sensing substrate with normal cells

HEK-293 T cells were used as "normal cells" in the present study. These cells are known to exhibit low to negligible folate receptor expression, making them suitable as a negative control.[41] HEK-293 T cells were obtained from the Cell Line Repository at the National Centre for Cell Sciences (NCCS, Pune, India), originally sourced from ATCC and authenticated by mitochondrial DNA analysis. Upon receipt, the cells were briefly cultured to prepare frozen stocks and stored in liquid nitrogen. For experiments, the cells were thawed and passaged prior to use. The HEK-293 T cells were maintained in DMEM supplemented with 10% FBS, 100 U $mL^{-1}$ penicillin G, and 100 μg $mL^{-1}$ streptomycin at 37 °C in a humidified 5% $CO_2$ incubator. To evaluate the specificity of the FA@GNP-coated sensing substrate, normal cells were applied to the substrate and observed by polarizing optical microscopy (POM). After coating, the substrate was subjected to a washing step to remove any unbound cells. The resulting image, as shown in Fig. 12(A), reveals a uniform dark pattern across the substrate, indicating the absence of bound cells and confirming that normal cells do not adhere to the FA@GNP-coated surface. In contrast, when normal cells were applied to the FA@GNP-coated substrate without subsequent washing, the substrate exhibited a bright texture, as illustrated in Fig. 12(B). This bright appearance is indicative of the presence of cells on the substrate surface, suggesting that normal cells adhere to the substrate initially but are removed upon washing.

The difference between the dark pattern observed after washing and the bright texture observed before washing validates that the FA@GNP-coated substrate does not bind to normal cells. This observation underscores the selective binding capability of FA@GNPs, which preferentially interact with colon cancer and breast cancer cells. Thus, the specificity of the substrate for cancer cells is affirmed, supporting its potential use in targeted cancer cell detection applications.

The cell detection platform is not able to discern distinct optical signals between HT-29 and MDA-MB-231 cells when incubated simultaneously, as shown in Fig. (13). This limitation arises because the optical signal observed under polarized optical microscopy (POM) is primarily due to the birefringence property of the liquid crystal (LC) molecules. The presence of cancer cells, regardless of the type, disrupts the molecular orientation of the LC layer, causing the incident light to split and produce a birefringent signal. Given that both HT-29 and MDA-MB-231 cells induce similar disruptions in LC alignment, the resulting optical signals are not cell-type specific.

### 3.11 Advantages and sensitivity of FA@GNP-based liquid crystal cell detection platform for cancer detection compared to existing technologies

The comparative Table 1 highlights the progress and effectiveness of various liquid crystal (LC) biosensors for detecting different cancer cell types, each employing distinct recognition elements to achieve high sensitivity and specificity. In this context, our LC-based detection platform, functionalized with folate-conjugated gold nanoparticles (FA@GNPs), demonstrates an impressive detection capability of 5–8 cancer cells per μL for both colon and breast cancer cells. This performance is noteworthy when compared with other LC biosensors targeting HER-2 biomarkers, CA125, or EpCAM-positive cancer cells, which, although sensitive, report detection limits in the range of 1 fg $mL^{-1}$ to 5 cells.

The incorporation of FA@GNPs offers distinct advantages over conventional recognition elements such as antibodies

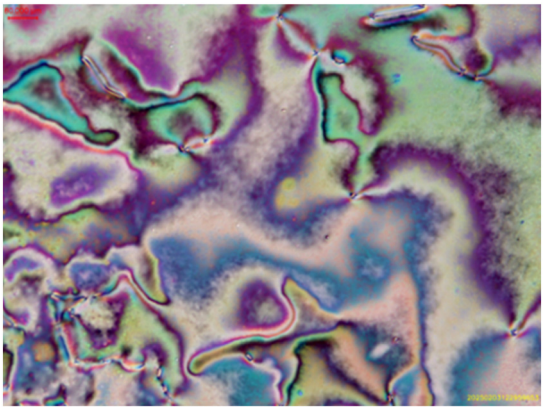

Fig. 13 POM image of HT-29 cells and MDA-MB-231 cells together in the LC cell detection platform.

and aptamers. Folate receptors are abundantly overexpressed on the surface of many malignant cells, enabling highly specific receptor–ligand interactions that facilitate selective binding. This biomolecular recognition imparts superior selectivity and binding stability, even under conditions where antibody- or aptamer-based systems may be less robust. The ability of the FA@GNP-LC biosensor to detect individual cancer cells underscores its exceptional sensitivity, which is crucial for early diagnosis and timely therapeutic intervention. Furthermore, the versatility of this platform in detecting both colon and breast cancer cells expands its diagnostic utility, positioning it as a promising tool for early cancer detection.

It is important to emphasize that the present study establishes the detection capability of the FA@GNP-functionalized LC biosensor in a DMSO-based medium, which provides a controlled environment to elucidate the fundamental sensing mechanism. Although clinically relevant biological matrices such as serum and blood may introduce additional challenges, including matrix interference and non-specific adsorption, the high sensitivity achieved here demonstrates the robustness and translational promise of this sensing approach. Future investigations will focus on optimizing the platform and validating its performance in complex biological fluids to advance its potential for real-world clinical applications.

## 4. Conclusion

In this study, we introduced a novel, highly sensitive, and label-free liquid crystal (LC) cell detection platform for cancer cells utilizing folate-conjugated gold nanoparticles (FA@GNPs) as the recognition element. This cell detection platform capitalizes on the overexpression of folate receptors on colon and breast cancer cells, enabling high-affinity binding between folate and these cancer cells. This specific interaction results in changes to the surface topography and disrupts the homeotropic orientation of the liquid crystal molecules, which can be distinctly observed under polarized optical microscopy. Our cell detection platform demonstrates exceptional sensitivity, with the ability to detect as low as a single cancer cell for both colon and breast cancers. This sensitivity represents a significant advancement over existing LC cell detection platforms, which generally achieve detection limits ranging from 1 fg $mL^{-1}$ to 5–8 cancer cells per μL for various biomarkers and cell types. The FA@GNP-based cell detection platform surpasses these benchmarks, offering a detection limit of 1 cancer cell, thereby setting a new standard in cancer diagnostics. The strategic use of FA@GNPs ensures unparalleled specificity and stability by targeting the folate receptors predominantly expressed on cancer cells, addressing the limitations faced by other recognition elements such as antibodies and aptamers. This high specificity translates into reliable and precise cancer cell detection under physiological conditions, enhancing the capability for early diagnosis. Furthermore, the versatility of this cell detection platform in detecting both colon and breast cancer cells broadens its diagnostic utility, presenting a powerful tool for early cancer detection and monitoring. The exceptional sensitivity, selectivity, and versatility of the FA@GNP-based LC cell detection platform highlight its transformative potential, paving the way for more effective and timely cancer diagnostics and management. One of the limitations of our study is that we did not evaluate how the washing step affects the results. In our study, we kept washing conditions consistent throughout our experiments (using the same buffer volume and flow rate); however, we did not thoroughly investigate how different washing intensities might influence our measurements. Understanding the relationship between washing strength and detection signal would provide valuable insights into the behaviour of the system. This gap in our methodology underscores the importance of developing standardized washing protocols for liquid crystal-based detection platforms to ensure the reliability and reproducibility of our findings in the future. Future work should address this variable more systematically to strengthen the robustness of this detection approach.

Table 1 Comparative table of liquid crystal biosensors for cancer cell detection

| Biosensor type | Cancer cell type | Recognition element | Detection limit | Ref. |
|---|---|---|---|---|
| Liquid crystal | HER-2 cancer biomarkers | HER-2 cancer antibodies | 1 fg $mL^{-1}$ | 20 |
| Liquid crystal | Cancer biomarker CA125 | Anti-CA125 antibodies | $10^{-10}$ g $mL^{-1}$ | 15 |
| Liquid crystal | EpCAM-positive cancer cells | EpCAM-specific aptamer | 5 cancer cells | 16 |
| Liquid crystal | Cancer biomarker CA125 | Anti-CA125 antibody | 0.01 ng $mL^{-1}$ | 17 |
| Liquid crystal | Colon cancer and breast cancer | Folate-conjugated gold nanoparticles | 5–8 cancer cell per μL | **Present work** |

## Conflicts of interest

All authors disclose no conflicts of interest.

## Data availability

Supplementary information is available. See DOI: **https://doi.org/10.1039/D5SD00111K**.

## Acknowledgements

Author Anupama Kadam acknowledges the "CHHATRAPATI SHAHU MAHARAJ NATIONAL RESEARCH FELLOWSHIP 2020, SARTHI (CSMNRF-2020, SARTHI)" for providing financial assistance. RP acknowledges the help from Dr. Mittal and Dr. Vaish, Department of Biotechnology, SPPU. AK acknowledges Dr. Nikhil Baban Ghate, Scientist "C" from BRIC-National center for cell science, Pune.

## References

1 Cancer. **https://www.who.int/news-room/fact-sheets/detail/cancer**.
2 A. Sakr, N. Soliman, M. Al-Gaashani, P. Pławiak, A. Ateya and M. Hammad, *Appl. Sci.*, 2022, **12**, 8450.
3 P. Jaglan, R. Dass and M. Duhan, *Journal of The Institution of Engineers (India): Series B*, 2019, **100**, 379–386.
4 L. Shen, L. Margolies, J. Rothstein, F. Eugene, M. Russell and S. Sieh, *Sci. Rep.*, 2019, **9**, 12495.
5 L. Nassif, M. Talib, Q. Nasir, Y. Afadar and O. Elgendy, *Artif. Intell. Med.*, 2022, **127**, 0933–3657.
6 E. Übeyli, *Expert Syst. Appl.*, 2007, **33**, 1054–1062.
7 M. Khalid, S. Deivasigamani, V. Sathiya and R. Surendran, *Sci. Rep.*, 2024, **14**, 19109.
8 S. Mohammadreza, M. Mohammad, G. Ali, E. Mahboube, K. Mishar, S. Hosna, A. Isa, C. Fatemeh, H. Hassan and S. Hosein, *Biosens. Bioelectron.*, 2024, **245**, 115818.
9 S. Xiuxia, H. Wenjing, Y. Dong, L. Chonglin and X. Jia, *Talanta*, 2019, **203**, 203–209.
10 D. JiaYin, J. QiFeng, L. XiaoChen, C. LongCong, Z. Yan and X. XingLiang, *Analyst*, 2019, **144**, 1761–1767.
11 Y. Shengyuan, L. Yanmei, T. Hui, W. Chao, W. Zhaoyang, S. Guoli and Y. Ruqin, *Chem. Commun.*, 2012, **48**, 2861–2863.
12 M. Khan, A. Khan, J. Shin and P. Soo-Young, *Sci. Rep.*, 2016, **6**, 22676.
13 K. Mashooq and P. Soo-Young, *Anal. Chem.*, 2014, **86**, 1493–1501.
14 X. Su, J. Xu, J. Zhang, D. Yang, W. Huo and C. He, *Liq. Cryst.*, 2020, **47**, 1794–1802.
15 Z. Jiao, S. Xiuxia, Y. Dong and L. Chonglin, *Talanta*, 2018, **186**, 60–64.
16 N. Rajib, L. Lisha, D. Joydip, J. Varsha and P. Santanu, *Analyst*, 2019, **144**, 1110–1114.
17 V. Sharma, A. Kumar, P. Ganguly and M. Biradar, *Appl. Phys. Lett.*, 2014, **104**, 043705.
18 M. Tyagi, A. Chandran, T. Joshi, J. Prakash, V. Agrawal and M. Biradar, *Appl. Phys. Lett.*, 2014, **104**, 154104.
19 H. Pham and J. Chang-Hyun, *Anal. Biochem.*, 2020, **593**, 113589.
20 H. Pourasl, A. Vahedi, H. Tajalli and B. Farzaneh, *Sci. Rep.*, 2023, **13**, 6847.
21 S. Hassanein, L. Mon-Juan and L. Wei, *Biosensors*, 2021, **11**, 271.
22 C. Tsung-Keng, T. Pei-Chi, L. Mon-Juan and L. Wei, *Biosens. Bioelectron.*, 2022, **216**, 114607.
23 H. Su, M. Lee and W. Lee, *J. Biomed. Opt.*, 2015, **20**, 57004.
24 A. Mansoori, S. Brandenburg and A. Shakeri-Zadeh, *Cancers*, 2010, **2**, 1911–1928.
25 M. Fernández, F. Javaid and V. Chudasama, *Chem. Sci.*, 2018, **9**, 790.
26 S. O. Alhaj-Suliman, I. Wafa and K. Salem, *Adv. Drug Delivery Rev.*, 2022, **189**, 114482.
27 E. Bellotti, M. Cascone, N. Barbani, D. Rossin, R. Rastaldo, C. Giachino and C. Cristallini, *Biomedicines*, 2021, **21**, 1275.
28 K. R. Kalli, *et al.*, *Clin. Cancer Res.*, 2008, **14**, 6530–6537.
29 Y. Lu, *et al.*, *Cancer Lett.*, 2013, 334.
30 D. Wenchao, Z. Peina, L. Yijing, X. Haibing, W. Dayang and T. Xutang, *ChemPhysChem*, 2015, **16**, 445–447.
31 A. V. Singh, H. Jungnickel, L. Leibrock, J. Tentschert, P. Reichardt, A. Katz, P. Laux and A. Luch, *Sci. Rep.*, 2020, **10**, 261.
32 C. Chen, J. Ke, X. Zhou, Y. Wei, B. Joseph, L. Jun, Y. Eu-Leong, H. X. Eric and M. Karsten, *Nature*, 2013, **500**, 486–489.
33 S. Mahalunkar, A. S. Yadav, M. Gorain, V. Pawar, R. Braathen, S. Weiss, B. Bogen, S. W. Gosavi and G. C. Kundu, *Int. J. Nanomed.*, 2023, **18**, 1607–1625.
34 A. V. Singh, G. Bansod, A. Schumann, F. S. Bierkandt, P. Laux, S. V. Nakhale, A. Shelar, R. Patil and A. Luch, *Curr. Anal. Chem.*, 2024, **20**(8), 988–1004.
35 M. Adabi, M. Naghibzadeh, M. Adabi, M. A. Zarrinfard, S. S. Esnaashari, A. M. Seifalian, R. Majidi, H. T. Aiyelabegan and G. Hossein, *Artif. Cells, Nanomed., Biotechnol.*, 2016, **45**(4), 833–842.
36 S. Yingze, Y. Jinhong, Y. Lianghao, E. A. Fakhr, D. Wen, L. Chaoyang and J. Nan, *Mater. Des.*, 2015, **88**, 950–957.
37 V. Yadav, V. Budhwar and M. Choudhary, *sian J. Pharm. Pharmacol.*, 2019, **5**, 682–692.
38 S. Yallappa, J. Manjanna, B. L. Dhananjaya, U. Vishwanatha, B. Ravishankar and H. Gururaj, *J. Mater. Sci.:Mater. Med.*, 2015, **26**, 235.
39 B. G. Linda, C. M. Stelia and M. O. Fernando, *J. Mex. Chem. Soc.*, 2018, **62**, 1–9.
40 A. V. Singh, T. Jahnke, S. Wang, Y. Xiao, Y. Alapan, S. Kharratian, M. C. Onbasli, K. Kozielski, H. David, G. Richter, J. Bill, P. Laux, A. Luch and M. Sitti, *ACS Appl. Nano Mater.*, 2018, **1**(11), 6205–6216.
41 A. R. Hilgenbrink and P. S. Low, *J. Pharm. Sci.*, 2005, **94**(10), 2135–2146.